



Strategy for improving photocatalytic ozonation activity of g-C₃N₄ by halogen doping for water purification

Yushan Tan, Weirui Chen*, Gaozu Liao, Xukai Li, Jing Wang, Yiming Tang, Laisheng Li*

School of Environment, South China Normal University, Key Laboratory of Theoretical Chemistry of Environment, Ministry of Education, Guangdong Provincial Engineering Technology Research Center for Drinking Water Safety, Guangdong Provincial Key Lab of Functional Materials for Environmental Protection, Guangzhou 510006, China

ARTICLE INFO

Keywords:
Photocatalytic ozonation
g-C₃N₄
Halogen doping
ATZ degradation

ABSTRACT

Feasibility of improving photocatalytic ozonation (PCO) activity of g-C₃N₄ (CN) by doping halogen (F, Cl, Br and I) was evaluated from the aspect of O₃/O₂ mass transfer and photogenerated electron (e⁻) and hole (h⁺) recombination. All halogen-CN had better activity (F-CN>I-CN>Cl-CN>Br-CN) for degrading ATZ than that of CN. Experimental and theoretical simulations results showed that doping halogen made the electron unevenly distributed and formed hydrophobic sites on CN, narrowed E_g of CN and enlarged e⁻ migration space. The above properties were favorable for enhancing mass transfer of O₃/O₂ and suppressed e⁻-h⁺ recombination. Besides, they either upshifted CB (C-I) or downshifted VB (C-F, C-Cl) to enhance the oxidation function of •OH or h⁺. One-electron reduction (high e⁻ utilization) of O₃ was weakened and three-electron reduction (low e⁻ utilization) of O₂ was enhanced with decrease of halogen electronegativity. This work provided insights into catalyst design for PCO process.

1. Introduction

The existence of trace pollutants had posed great threats to water quality. Atrazine (ATZ) was widely used as herbicide [1]. It had many adverse impacts on both environment and humankind. For instance, it was considered as an endocrine disruptor and would cause the feminization of frog [2,3]. Because of its stable covalent structure, ATZ was inert to conventional water treatment technology [4]. The cost-effective treatment was urgently needed.

Ozonation was the common water purification technology, which was normally employed for decolor, deodorize and decontamination [5]. However, restrained by the limited oxidation potential of O₃ (2.07 eV), sole ozonation was low in removing pollutants like ATZ [6]. At the same time, it would always generate toxic by-products, such as bromate. Moreover, the O₃ utility rate was also not high [7–9]. Various kinds of active solids were introduced to transform O₃ into secondary radicals with greater oxidation potential (mainly •OH, 2.78 eV) [10,11]. The above multi-phase system was known as catalytic ozonation, which was characterized for the higher O₃ utility rate, the greater pollutants removal and the less toxic by-products generation [12–14]. The active sites of ozonation catalyst were often related with electron-rich region like Lewis sites, oxygen vacancies, N vacancies, low valence metals [7].

For the reductive activation of O₃, electron was gradually migrated from catalysts to their surface bonded O₃. Unfortunately, the continuous loss of inherent electrons would inactivate catalysts (activators for more precisely) if no additional electron was supplied. Moreover, heterogeneous catalytic ozonation also suffered from the dilemmas of limited mass transfer of reactants, and the secondary pollution caused by leached metal [5]. In this regard, the combination of ozonation with photocatalysis, which was termed as photocatalytic ozonation (PCO), could be emerged as the cost-effective alternative for activating O₃ [15]. Similar with persulfate mediated photocatalysis process, during PCO process, O₃ also acted photogenerated electrons (e⁻) consumer and trapped e⁻ immediately, which formed •OH simultaneously [16]. Because the involved electron was excited by light, the inactivation of catalyst due to the loss of their inherit electron could be overcome. Moreover, due to the consumption of e⁻ by O₃, photogenerated holes (h⁺) had enough time to oxidize pollutants or transform H₂O into •OH when its oxidation potential was higher than that of H₂O/•OH [17]. Therefore, PCO could be regarded as cost-effective water treatment process both for overcoming the mentioned limitations of ozonation and h⁺-e⁻ recombination of photocatalysis. To this end, efficient semiconductor catalysts were required to provide abundant e⁻ for O₃'s activation process. For instance, catalysts with ultraviolet light response,

* Corresponding authors.

E-mail addresses: Chen_2019@m.scnu.edu.cn (W. Chen), lsh@scnu.edu.cn (L. Li).



such as Fe-CeO_{2- σ} , GO-TiO₂ etc, were designed and employed successfully in PCO for p-chlorophenol and primidone [15,18].

Because of the fact that ultraviolet light only accounted for 5% energy of solar light, catalysts with visible light (Vis) response had bright prospects in PCO process. g-C₃N₄ (CN) was a typical kind of Vis-response semiconductor, with s-triazine ring as basic unit and conduction band (CB) potential at -1.30 eV. Since O₃/•O₃⁻'s reduction potential was 1.6 eV, therefore, O₃ could capture and react with e⁻ easily [19]. Cao's group had done excellent works on the application of CN in PCO process and they thought that the reduction of O₃ into •OH by e⁻ followed the one-electron reduction pathway (SER, O₃ → •O₃⁻/HO₃ • → •OH) [19–21]. But we found that there still existed some limitations for CN based PCO: (1) N atoms in the bridge site, which connected three s-triazine rings, did not involve in the composition of neither conductive band (CB) nor valence band (VB) [22]. Therefore, h⁺-e⁻ could only separate and migrate in a s-triazine ring; (2) Considering the predominant amount of O₂ over O₃ in sparged gas, it should be noted that the excessive O₂ would also consume e⁻ via three-electron reduction pathway (TER, O₂ → •O₂⁻/HO₂ • → H₂O₂ → •OH), which was suggested as low utilization of e⁻ [19]. Moreover, hydrophilic CN had no selectivity towards O₃'s mass transfer, great deal of O₃ was not utilized [23]. The existing methods for improving behavior of catalysts were precious metal modification or building heterojunction [24,25]. These methods could only separate h⁺-e⁻ in a limited area on catalysts, the mentioned drawbacks were not well solved. Hence, we thought that: was it feasible to boost O₃'s mass transfer and enrich its surface concentration on CN

for the convenient consumption of e⁻ and generation of •OH?

Taking the hydrophobicity and electrophilicity of O₃ into consideration, we tried to build hydrophobic sites and make the electron unevenly distributed on CN by doping halogen (F, Cl, Br, I) into its framework. O₃ had high affinity toward hydrophobic areas and sites with rich electron. Chen et al. had found that F would replace Si-OH on MCM-41 and form the hydrophobic and electron withdrawing Si-F group to accelerate mass transfer of O₃ [26]. Hence, the hydrophobic carbon-halogen bond could also enhance the mass transfer of O₃, which accelerated SER reaction and improved utilization rate of O₃ and e⁻. Meanwhile, because of the difference in electronegativity, the introduction of halogens could redistribute the electron on CN. Therefore, h⁺-e⁻ could transfer between s-triazine rings, which reduced their recombination rate. In order to verify our proposal, ATZ was selected as model pollutant to explore the activity of halogen-CN in PCO process. Systematic experiments, characterizations and theoretical results were used to explore the reaction mechanism.

2. Experimental sections

Chemical regents, catalyst preparation, analysis and calculation methods were enclosed in [Supplementary materials](#).

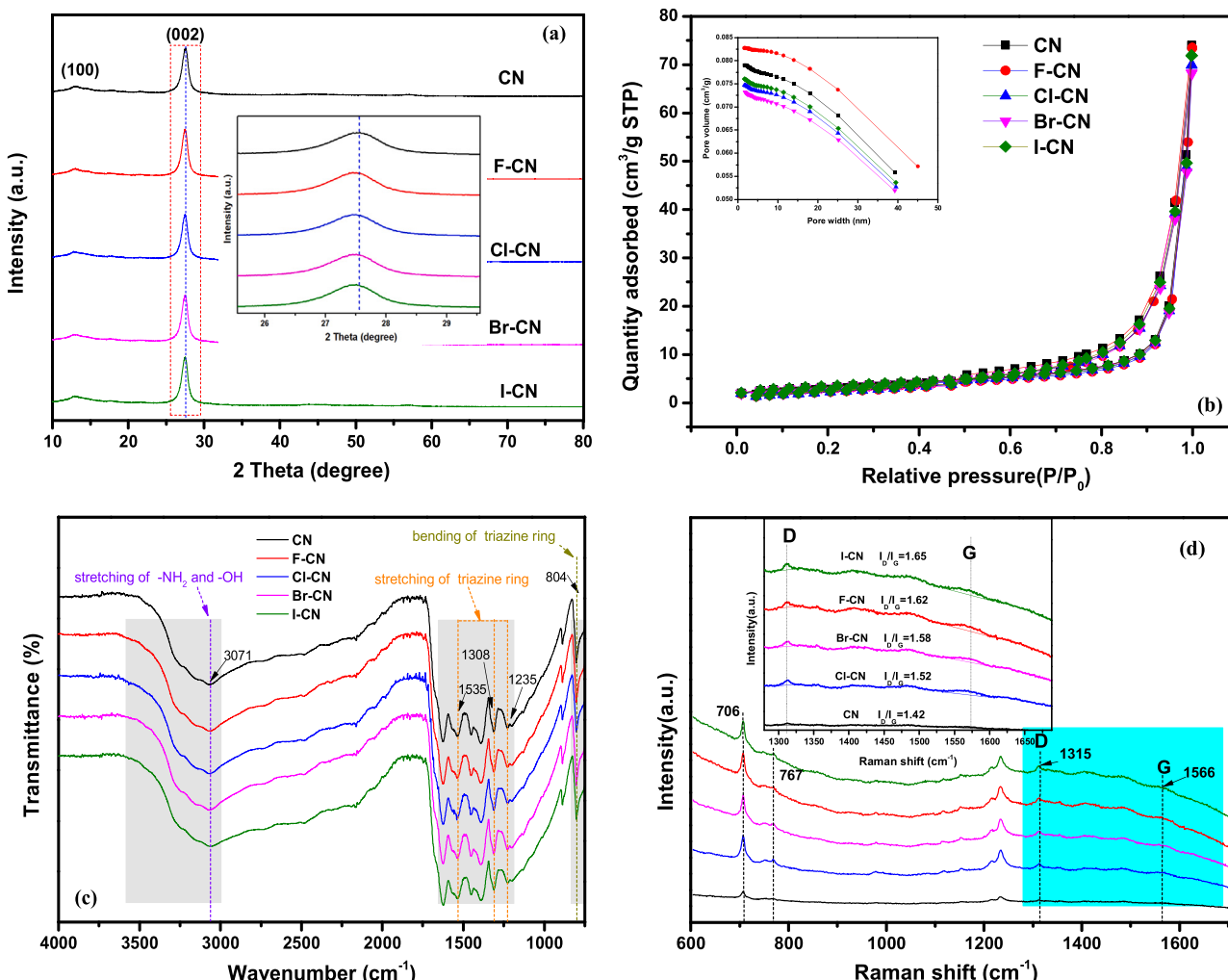


Fig. 1. (a) XRD, (b) N₂ adsorption-desorption isotherm, (c) FTIR and (d) Raman spectra of different CN.

3. Results and discussions

3.1. Characterizations of catalysts

The successful preparation of catalysts was confirmed by XRD. As exhibited in Fig. 1(a), there were a small peak at $2\theta = \sim 13.1^\circ$ and a strong peak at $2\theta = \sim 27.6^\circ$ for all CN based samples, which were corresponding to JCPDS Card 87-1526. Generally, the peak at $\sim 13.1^\circ$ was referred as (100) plane formed by s-triazine unit and the peak at $\sim 27.6^\circ$ was the (002) plane resulted from the accumulation of aromatic fragments [27]. Compared with pure CN, the doping of F, Cl, Br and I atom shifted the (002) plane to the lower angle ($\sim 27.4^\circ$), which suggested the increase of cell unit or inter planar spacing. Taking the atomic radius of F (0.68 nm), Cl (0.99 nm), Br (1.14 nm), I (1.46 nm) and N (0.74 nm) into consideration, Cl, Br and I should enlarge cell unit of CN because of their greater atomic radius than that of N. The doping of F ought to shift the (002) plane to the larger angle, but NH_3 (formed during hydrothermal of ammonium halide) would depart CN layer and increase inter planar spacing, which remedied the shrinking of cell unit. Morphologies of CN before and after halogen doping were recorded by TEM (Fig. S1). All samples presented the interlayer stacked structure and no difference was found, which indicated that the incorporation of halogen atoms did not damage CN's framework.

N_2 adsorption-desorption isotherms and FTIR results also verified that there was no obvious structural damage during modification. All N_2 adsorption-desorption isotherms were type III (Fig. 1(b)). As shown in Table 1, S_{BET} were measured as 11.6, 10.9, 11.4, 11.6 and 12.3 m^2/g for CN, F, Cl, Br and I-CN, respectively. S_{BET} discrepancies were within the error range, suggesting that the doping of halogens had no improvement on S_{BET} . As shown in Fig. 1(c), the bending mode of s-triazine ring had a peak at $\sim 804 \text{ cm}^{-1}$ and the stretching vibration at $\sim 1200\text{--}1650 \text{ cm}^{-1}$ [28,29]. The signal between 3000 and 3600 cm^{-1} was referred as the stretching vibration of $-\text{NH}_2$ and $-\text{OH}$ [30]. Because of the detection limitation of FTIR, no peak of C-X (X = F, Cl, Br, I) bond was detected for halogen-CN. All samples presented the similar FTIR spectra, which further confirmed that the structure of CN was not damaged after doping with halogens by hydrothermal treatment.

Raman spectroscopy and XPS were also carried out. As depicted in Fig. 1(d), two characteristic peaks at 706 and 767 cm^{-1} were found for all CN samples. The board peak at the range of $1000\text{--}2000 \text{ cm}^{-1}$ was resulted from the fluorescence absorption of conjugated layered structure. D band and G band could be observed at 1315 cm^{-1} and 1566 cm^{-1} , respectively. Generally, I_D/I_G ratio was used as index of C defects [31]. I_D/I_G ratio increased after halogen doping, which suggested that halogens would disorder the structure and enrich the surface defect. More information on C—X bond was illustrated by XPS. Besides C and N elements, halogen atoms were also detected in the XPS survey with F 1 s centering at $\sim 698.0 \text{ eV}$, Cl 2p centering at $\sim 197.5 \text{ eV}$, Br 3d centering at $\sim 69.2 \text{ eV}$, I 3d centering at $\sim 620.0 \text{ eV}$ (shown in Fig. S2). And the exact incorporated amount halogen was 0.61% for F-CN, 0.13% Cl-CN, 0.10% Br-CN and 0.07% I-CN (Table S1). As shown in Fig. 2(a), C1s of CN was deconvoluted into superficial amorphous C (C-C/C=C, $\sim 284.8 \text{ eV}$), C-O of surface absorbed-H₂O ($\sim 286.1 \text{ eV}$) and the sp² hybridization in s-triazine units (N—C=N, $\sim 288.5 \text{ eV}$) [32]. After doping with halogens, four new peaks at 289.5, 286.3, 285.8 and 285.7 eV, which were corresponded to C-F, C-Cl, C-Br and C—I bond, occurred for

F-CN, Cl-CN, Br-CN and I-CN, respectively (Enlarged figures could be found at Fig. S3) [33,34]. Compared with that of CN, binding energy of the N—C≡N peak on F-CN became larger but it shifted to the lower binding energy for the case of Cl, Br and I-CN. As for N 1s spectrum (Fig. 2(b)), it was deconvoluted into four peaks centering at $\sim 398.8 \text{ eV}$ (sp² hybrid N (C=N=C)), $\sim 399.6 \text{ eV}$ (bridged N (N-(C)₃)), $\sim 401.2 \text{ eV}$ (N—H bond), and $\sim 404.2 \text{ eV}$ ($\pi\text{-}\pi^*$ excitation between stacked layers) [32]. After doping with halogens, both C-N=C and N-(C)₃ peaks of F-CN shifted to the larger binding energy but they shifted to the lower binding energy for Cl-CN, Br-CN and I-CN. F had the strongest electronegativity (3.98), therefore, part of the electrons on bulk CN were withdrawn by F, which led to the shift of N—C≡N, C=N=C and N-(C)₃ peaks to the greater binding energy. With the increase of atomic number, the electronegativity of Cl (3.16), Br (2.96) and I (2.66) decreased. Therefore, the inherent electron of Cl, Br and I would migrate to bulk CN, which resulted in the shift of characteristic peaks to the lower binding energy [22]. N-(C)₃% and C=N=C% were also calculated to investigate the incorporation sites of halogens. N-(C)₃% and C=N=C% was 55.2% and 33.1% for CN. N-(C)₃% decreased to 26.8% after doping by F, which verified the replacement of N with F. Similarly, C=N=C% decreased to 41.3%, 48.9% and 43.1% after doping with Cl, Br and I, respectively. The decline of C=N=C% indicated the replacement of edge N by Cl, Br and I. Two peaks with chemical shift of ~ 150.0 and $\sim 161.1 \text{ ppm}$ were observed in ¹³C NMR spectrum (Fig. 2(c)). The chemical shift was in the scope of ab initio calculations results, which verified the heptazine unit in CN polymer (Fig. 2(e)) [35]. The peak at $\sim 150.0 \text{ ppm}$ was attributed to tri-coordinate carbon (C_i) within the s-triazine ring and the chemical shift of $\sim 161.1 \text{ ppm}$ was the tri-coordinate (C_e) carbon connected to another s-triazine ring [36]. As for ¹⁵N NMR spectrum (Fig. 2(d)), four characteristic peaks were observed at chemical shift of ~ 113.8 , ~ 136.0 , ~ 162.9 and $\sim 194.6 \text{ ppm}$, which were attributed to terminal N (N_{t2H}), bridge N (N_{tH}), central N (N_i) and edge N (N_e) [35,37]. Intensity of central N (N_i) and edge N (N_e) for F, Cl, Br and I-CN decreased when compared with that of CN, which suggested the potential substitution of central N and edge N with F/Cl/Br/I atom. NMR results were consistent with XPS results and they all confirmed the successful preparation of CN and halogen-CN.

DFT calculation was performed to further investigate doping sites of halogen and their influence on lattices parameters. The in-plane lattice constant of the optimized structure of monolayer CN was 7.12 Å, which was consistent with reported literatures [22]. As shown in Fig. 3(a), there were three types of N atoms (named as N1, N2 and N3) and two types of C atoms (named as C1 and C2) in CN. N1—C2, C2—N2, N2—C1 and C1—N3's bond lengths were 1.39, 1.33, 1.33 and 1.47 Å, respectively. The most favorable site for halogens atoms doping were investigated by calculating their formation energy (Text S1). According to the definition of formation energy, the substitutable positions for halogens were the site with the smallest formation energy.

As depicted in Fig. 3(b-e) and Table 2, F was more likely to replace N1 (namely central N) whereas Cl, Br, and I were more likely to incorporate at N2 (namely edge N) sites both for C and N rich environment. Lengths of C1-N3, C2-N2, N2-C1 and N1-C2 were shorten after halogens doping while the C-X (X=F, Cl, Br and I) were enlarged when compared with C-N of CN (Table S2).

3.2. Photocatalytic ozonation processes

Fig. 4(a) showed that after the doping of halogens into CN, PCO efficiencies toward ATZ were enhanced in different degrees. ATZ removals in 15 min and the first order kinetic rate constants were in the order of: O₃/Vis/F-CN (66.5%, 0.0695 min^{-1}) > O₃/Vis/I-CN (61.2%, 0.0637 min^{-1}) > O₃/Vis/Cl-CN (57.1%, 0.0573 min^{-1}) > O₃/Vis/Br-CN (49.8%, 0.046 min^{-1}) > O₃/Vis/CN (44.0%, 0.0392 min^{-1}). Taking the exact incorporated amount of halogen into consideration, I-CN still had the better activity than those of Cl, Br-CN though they had the similar atomic percentage. Moreover, their activity order during PCO

Table 1
Textual properties of CN and halogen-CN.

Catalysts	S_{BET} (m^2/g)	Pore size (nm)	Pore volume (cm^3/g)
CN	11.6	10.9	0.032
F-CN	10.9	11.1	0.030
Cl-CN	11.5	10.6	0.030
Br-CN	11.6	10.3	0.029
I-CN	12.3	10.1	0.031

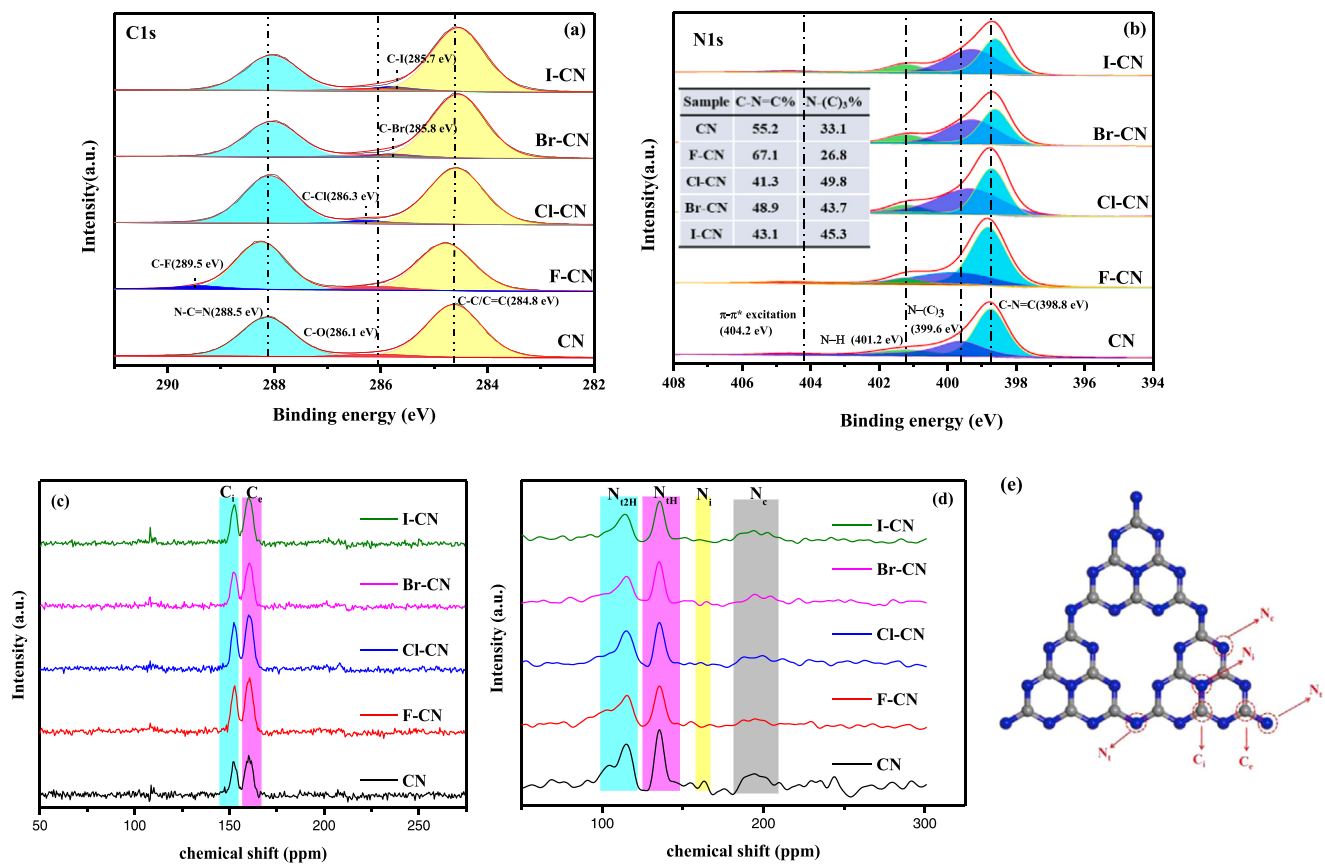


Fig. 2. (a) C 1s pattern, (b) N 1s pattern, (c) ^{13}C NMR, (d) ^{15}N NMR of different CN and (e) basic unit of CN.

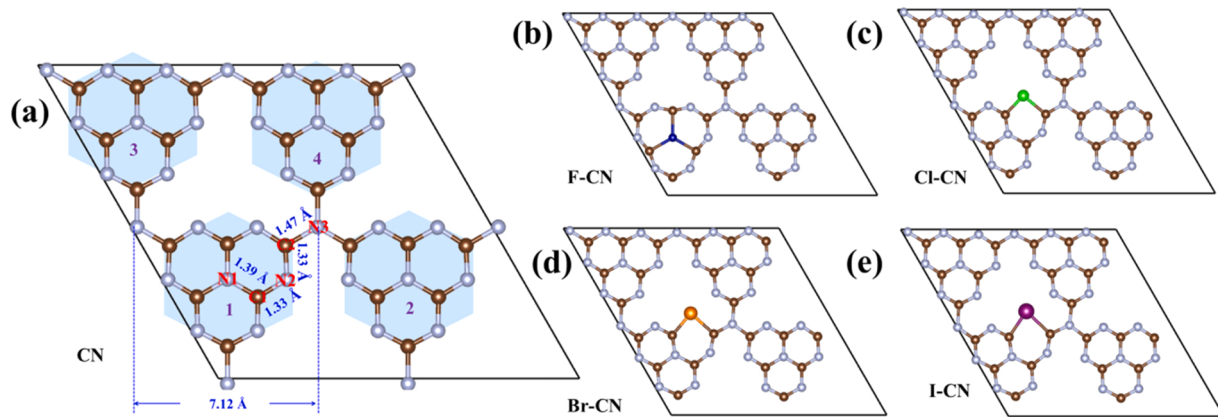


Fig. 3. Optimized structure of (a) CN, (b) F-CN, (c) Cl-CN, (d) Br-CN and (e) I-CN.

Table 2
Formation energy of halogens doping.

Doping sites	F		Cl		Br		I	
	C-rich	N-rich	C-rich	N-rich	C-rich	N-rich	C-rich	N-rich
C1	5.80	6.45	6.49	7.14	7.58	8.23	8.84	9.49
C2	2.74	3.39	5.77	6.42	7.72	8.37	5.13	5.78
N1	1.53	1.05	6.80	6.31	9.44	8.95	11.71	11.23
N2	1.96	1.48	3.72	3.23	4.43	3.94	4.84	4.35
N3	5.48	5.00	8.31	7.82	10.15	9.66	12.67	12.18

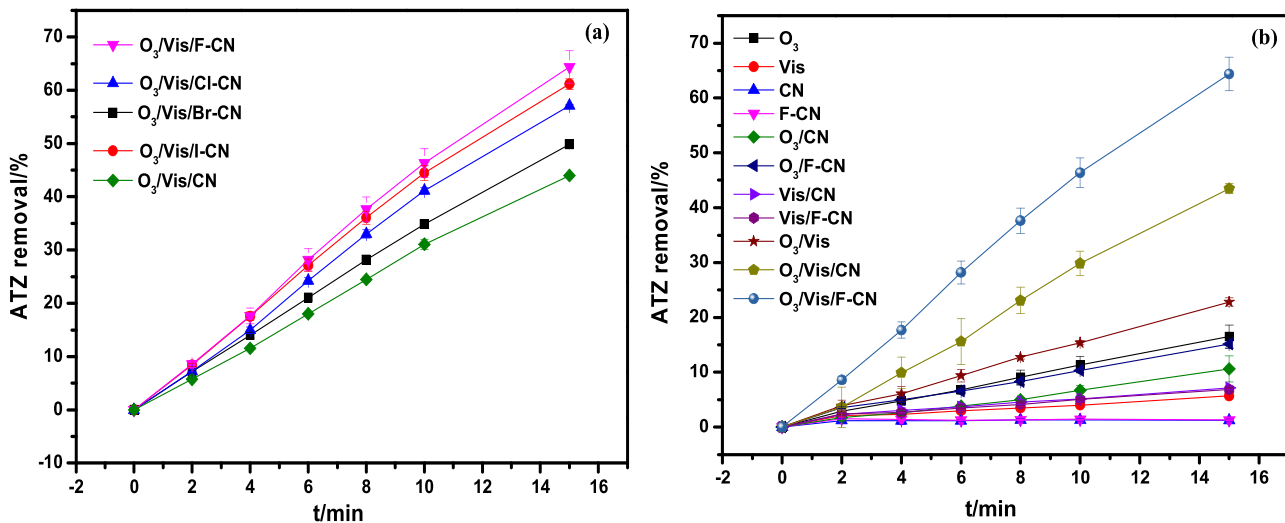


Fig. 4. (a) Influence of halogen type on ATZ removal; (b) Systematically comparison of ATZ degradation by O₃/Vis/F-CN process; Reaction parameters: dosage of catalyst: 0.2 g/L; ATZ concentration: 10 mg/L; volume: 700 mL; temperature: 25 °C.

was also inconsistent with order of halogen incorporated amounts. For the deeper exploration of the function of halogens in CN, the more detailed comparisons were made among O₃, Vis, O₃/Vis, Vis/catalysts, O₃/catalysts, O₃/Vis/catalysts. Taking O₃/Vis/F-CN system as example (shown in Fig. 4(b)), no ATZ adsorptions were found by both CN and F-CN. Sole ozonation, Vis/CN and Vis/F-CN were low efficiency in degrading ATZ, with only 14.9%, 6.9% and 7.1% ATZ removals were obtained. The combinations of O₃ with CN or F-CN were also not ideal. But ATZ removal in O₃/F-CN (15.1%) was greater than that of O₃/CN (10.0%). This increase was due to generation of greater amount of C=O groups during the modification process, which was favorable for activating O₃ [38]. The most remarkable improvement of ATZ degradation was observed after coupling ozonation with Vis/CN or Vis/F-CN process. About 44.0% removal rates were achieved in O₃/Vis/CN process and it further boosted to 66.5% for O₃/Vis/F-CN process. Influences of environmental engineering factors were also considered. As shown in Fig. S4 (a), (b), ATZ removal gradually increased with dosage of F-CN. The greatest ATZ removal was 69.5% when F-CN's dosage reached 0.4 g/L. ATZ removals were also enhanced with O₃ dosage. About 83.0% ATZ was removed in 15 min when O₃ dosage reached 60 mg/h. The above enhancements were due to the exposure of greater active sites and the existence of greater amount of e⁻ consumer, which increased light penetration and adsorption, suppressed h⁺-e⁻ combination and generated greater amount of •OH. The influence of initial pH on ATZ removal was investigated. As shown in Fig. S4(c), ATZ removal in O₃/Vis/F-CN process increased with initial pH value, which could be attributed to the accelerated activation of O₃ into •OH by OH⁻. The maximum removal efficiency was 88.9% at pH=9. The feasibility of O₃/Vis/F-CN in real water was also explored. The water from Guanzhou River (Guangzhou City, Guangdong Province, China) was used as reaction medium and the water quality parameters were depicted in Table S3. Compared with the deionized water as reaction medium, ATZ removal decreased from 44.0% to 39.9% for O₃/Vis/CN and from 66.5% to 57.2% for O₃/Vis/F-CN when using Guanzhou River as reaction medium (Fig. S4(d)). F-CN still had the greater performance over CN in real water medium. The decrease of performance could be attributed the competition for ROSs by inorganic and organic matter such as NO₃⁻, SO₄²⁻ and natural organic matters [39].

Synergy factor (η) was introduced to investigate the influence of halogen type. PCO process could be regarded as the coupling of ozonation (O) and photocatalysis (PC). After fitted with first-order-kinetic model, the reaction constant (k) was obtained and used to calculate η ($\eta = k_{\text{PCO}}/k_0 + k_{\text{PC}}$). As shown in Table 3, η increased in the order of O₃/

Table 3

First-order-kinetic rate constant of ozonation, photocatalysis and photocatalytic ozonation.

System	k_0 (min ⁻¹)	k_{PC} (min ⁻¹)	k_{PCO} (min ⁻¹)	η
O ₃ /Vis/CN	0.0119	0.0045	0.0392	2.38
O ₃ /Vis/F-CN	0.0119	0.0035	0.0695	4.52
O ₃ /Vis/Cl-CN	0.0119	0.0041	0.0573	3.59
O ₃ /Vis/Br-CN	0.0119	0.0046	0.0460	2.78
O ₃ /Vis/I-CN	0.0119	0.0028	0.0637	4.32

Vis/CN (2.38) < O₃/Vis/Br-CN (2.78) < O₃/Vis/Cl-CN (3.59) < O₃/Vis/I-CN (4.32) < O₃/Vis/F-CN (4.52). Because all CN based catalysts had the similar S_{BET} , therefore, the activity discrepancies could be attributed the change of chemical properties induced by halogen doping. Moreover, ATZ removals and η were not positive correlated with neither electronegativity nor incorporated amounts of investigated halogens, which suggested the existence of multiple factors for the improvement of CN's activity. The stability of halogen doped CN during PCO processes was also investigated. As shown in Fig. S5, during five times' successive use, about 5.56% decline of ATZ removal was observed for O₃/Vis/CN and about 4.27–8.06% in ATZ removal was found for halogen doped CN based PCO processes.

3.3. Reaction mechanism of photocatalytic ozonation

Basically speaking, PCO process still obeyed the rule of photocatalysis. The yields of h⁺-e⁻, separation of h⁺-e⁻, mass transfer of O₂/O₃ and their interfacial reaction with e⁻ as well as the oxidation of pollutant by reactive species were highly influential to the efficiency of PCO.

The amount of h⁺-e⁻ was dependent on the band gap (E_g) of semiconductor. UV-Vis diffuse reflectance spectrum of different CN catalysts (Fig. 5(a)) reflected that the doping of halogen atoms would result in the blue shift of CN. Tauc curves were also employed by plotting $h\nu$ vs $(\alpha h\nu)^{1/n}$ to study the E_g of catalysts. α was the absorbance coefficient, h was the Planck constant, ν was referred to frequency. n was 1/2 for indirect semiconductor and 2 for direct semiconductor. According to reported literatures, CN was the direct semiconductor and the halogen modified CNs were belonged to indirect semiconductor [22,40]. As shown in Fig. 5(b), E_g was 2.82, 2.61, 2.61, 2.61 and 2.62 eV for CN, F-CN, Cl-CN, Br-CN and I-CN, respectively. Compared with that of CN, halogen-CN had the narrower E_g, which indicated that they had the greater optical adsorption and the greater generation of h⁺-e⁻. As shown

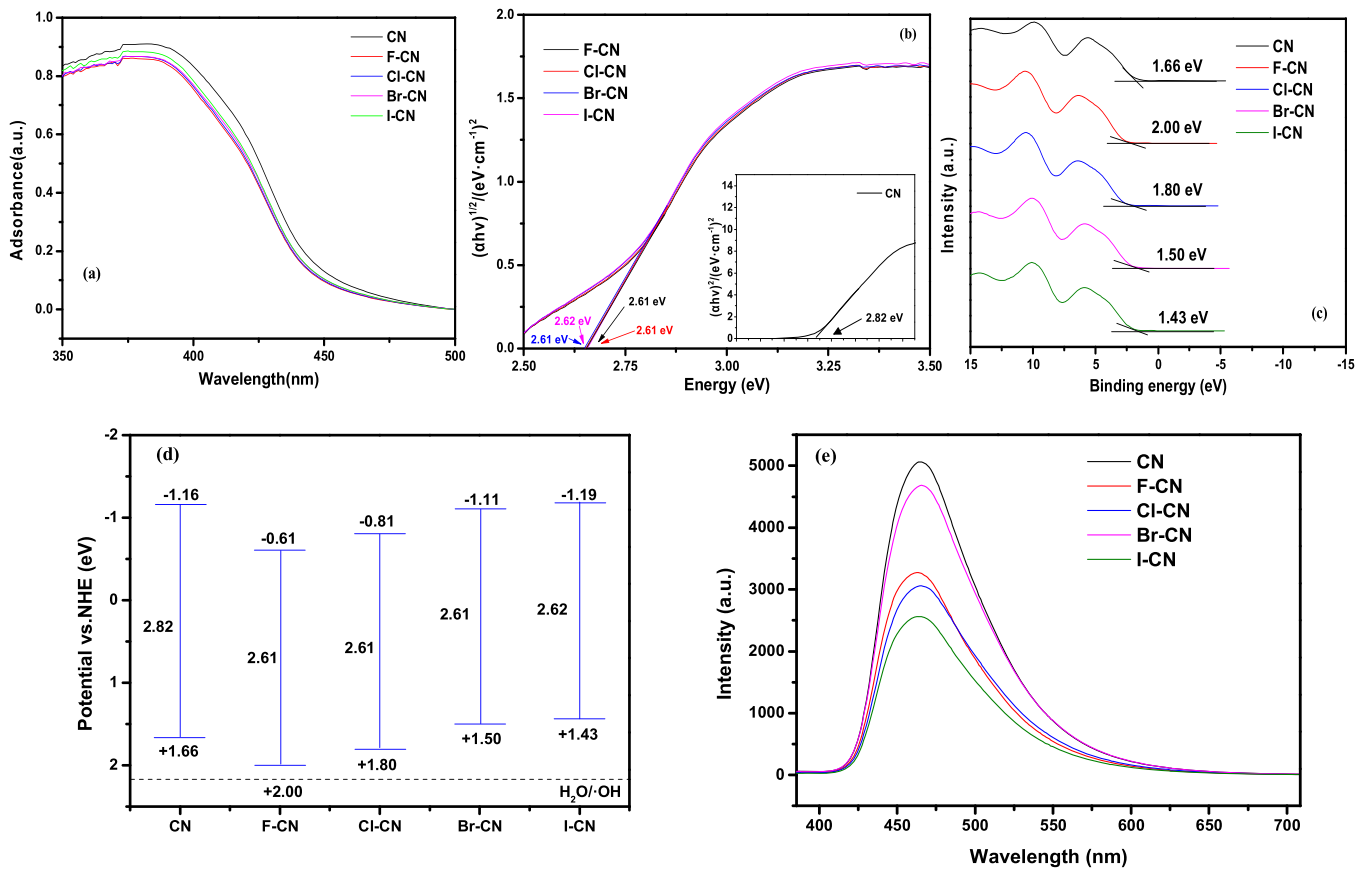


Fig. 5. (a) UV-vis DRS spectra; (b) Tauc plots; (c) VB XPS spectra; (d) Band structure; (e) PL spectra.

in Fig. 5(e), the fluorescence intensities (with emission wavelength at \sim 475 nm) of catalysts decreased obviously in the order of I-CN < Cl-CN < F-CN < Br-CN < CN. Generally speaking, the lower fluorescence intensity indicated the lower $h^+ - e^-$ recombination rate [41]. Therefore, it was reasonable to infer that e^- had the larger migration

space on halogen-CN than that on CN (proved by HOMO and LUMO calculation in latter parts). Fig. 5(c) was the VB XPS of five kinds of CN. VB potentials were measured as 1.66, 2.00, 1.80, 1.50 and 1.43 eV for CN, F, Cl, Br and I-CN, respectively. And their CB potentials were -1.16, -0.61, -0.81, -1.11 and -1.19 eV. VB potential was related with the

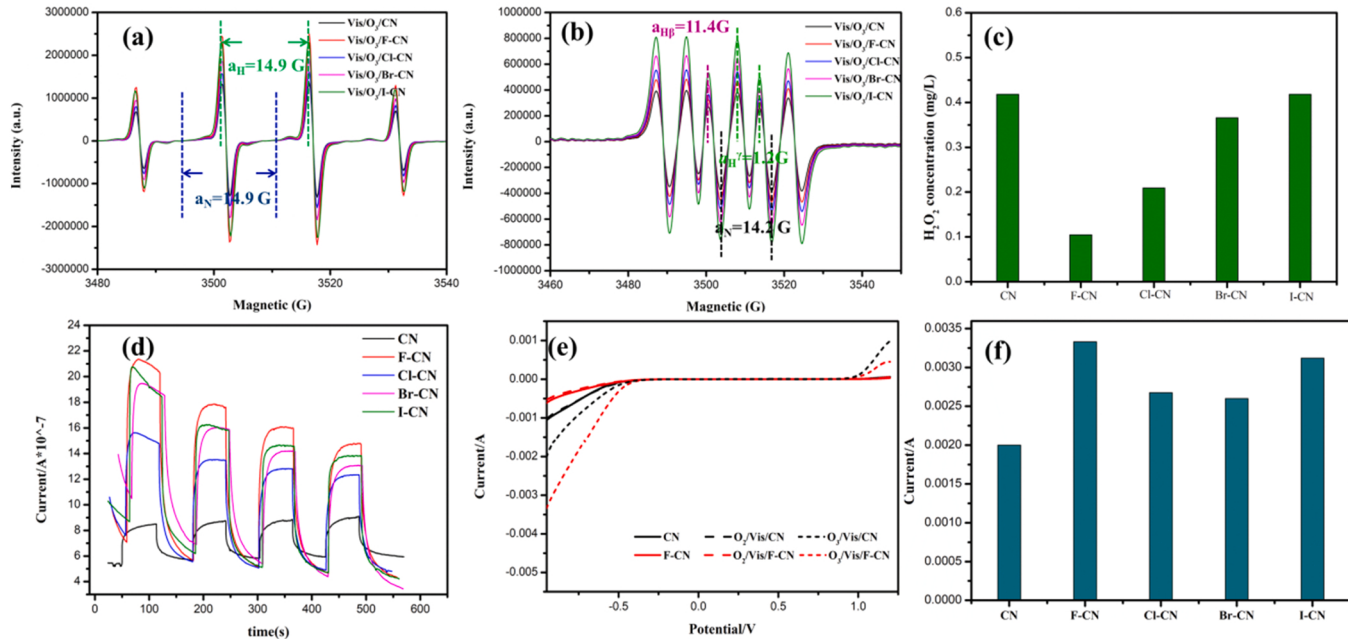
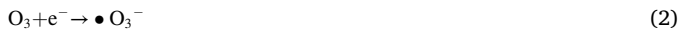


Fig. 6. EPR pattern of •OH-DMPO adducts (a) and •O₂-DMPO adducts (b), H₂O₂ generation (c), (d) photo-currents, (e) linear sweep voltammetry curve (LSV) characterization and (f) initial current of different PCO process.

oxidation capacity of h^+ . Generally, h^+ could oxidize the surface absorbed H_2O into $\bullet\text{OH}$ [42]. Meanwhile, it could also oxidize pollutant directly [43]. The oxidation potential of $\text{H}_2\text{O}/\bullet\text{OH}$ was 2.27 eV, which was much greater than the VB potential of CN and halogen-CN [43]. Therefore, the possibility of transforming H_2O into $\bullet\text{OH}$ by h^+ was excluded. Hence, the role of h^+ in this study was mainly referred as its direct oxidation of pollutant. As for photogenerated e^- , its reaction with O_2/O_3 was effected by the reductive capacity of CB [44]. Among the investigated CN and halogen-CN, I-CN possessed the lowest CB potential, which meant that the reaction between e^- with O_2/O_3 on I-CN was more favorable than other kinds of catalysts.

Based on the above discussions, the generation amount of $\bullet\text{OH}$, $\bullet\text{O}_2^-$ and H_2O_2 were recorded to interpret the reaction between O_3/O_2 with photogenerated e^- . EPR was conducted to detect $\bullet\text{OH}$ and $\bullet\text{O}_2^-$ with DMPO as trapping molecular. DMPO would react with $\bullet\text{OH}$ and generated $\bullet\text{OH}-\text{DMPO}$ complex, which presented the characteristic 1:2:2:1 pattern [45]. $\bullet\text{O}_2^-$ detection was conducted in methanol solution to inhibit the interference of $\bullet\text{OH}$ and the $\bullet\text{O}_2-\text{DMPO}$ normally exhibited sextet peaks [46]. As shown in Fig. 6(a), the $\bullet\text{OH}-\text{DMPO}$ adducts (hyperfine splitting couplings were $a_N = a_H = 14.9 \text{ G}$), were detected in all PCO processes and their signals were in the order of $\text{O}_3/\text{Vis/F-CN} > \text{O}_3/\text{Vis/I-CN} > \text{O}_3/\text{Vis/Br-CN} > \text{O}_3/\text{Vis/Cl-CN} > \text{O}_3/\text{Vis/CN}$. After removing dissolved O_3 by bubbling Ar into solution, the signal of $\bullet\text{OH}-\text{DMPO}$ adducts for all CN based photolysis processes were much less than those of PCO processes, which verified the essential existence of O_3 for generating $\bullet\text{OH}$ (Fig. S6). During PCO process, both O_3 and O_2 could serve as e^- consumer and generated $\bullet\text{OH}$ through SER or TER pathways, respectively [19]. Because of the impossibility for h^+ to oxidize H_2O into $\bullet\text{OH}$, $\bullet\text{OH}$ should be positive correlated with CB potential. As shown in Fig. 5(d), CB potential was in the order of I-CN>Br-CN>Cl-CN>F-CN>CN. F-CN had the lowest CB position but $\text{O}_3/\text{Vis/F-CN}$ process had the greatest $\bullet\text{OH}$ amounts, which indicated that other factors should be considered for generating $\bullet\text{OH}$ besides the band position of catalysts. Carbon halide bond was known as hydrophobic [47]. Hence, halogen modified CN should have the better affinity towards O_3 and O_2 than that of CN. Among the investigated halogens, F had the strongest electronegativity and the formed C-F zone would withdraw electron from the s-triazine ring and construct the zone with rich electron, which endowed F-CN with selectiveness toward electrophilic O_3 [48]. Eqs. (1)–(8) indicated that the theoretical e^- consumption for reducing O_3 into $\bullet\text{OH}$ was one third of reducing O_2 into $\bullet\text{OH}$. Therefore, O_3 could utilize e^- more efficiently and generate more $\bullet\text{OH}$. The inconsistent order between CB potential and $\bullet\text{OH}$ amount suggested that the enhanced mass transfer of O_3 could compensate for the increase of CB potential.



The sextet signals (hyperfine splitting constants of $a_N = 14.2 \text{ G}$, $a_H^\beta = 11.4 \text{ G}$, and $a_H^\gamma = 1.2 \text{ G}$), which were characteristic for $\bullet\text{O}_2^-$ -DMPO adducts, were detected for all PCO processes and their intensities were in the order of $\text{O}_3/\text{Vis/I-CN} > \text{O}_3/\text{Vis/Br-CN} > \text{O}_3/\text{Vis/Cl-CN} > \text{O}_3/\text{Vis/F-CN} > \text{O}_3/\text{Vis/CN}$ (Fig. 6(b)). As discussed in former parts, $\bullet\text{O}_2^-$ was an

important intermediate of O_2 's TER reaction (Eqs. (5)–(8)) [19]. Hence, the tendency of $\bullet\text{O}_2^-$ amounts in halogen-CN PCO processes suggested that the possibility of TER reaction between e^- and O_2 increased with atomic number of halogens. As proposed in former parts, C-F groups, which endowed g-C₃N₄ the selective affinity towards O_3 by the electron-rich zone, could reduce the inefficient use of photogenerated e^- by O_2 . Therefore, $\text{O}_3/\text{Vis/F-CN}$ had the smallest $\bullet\text{O}_2-\text{DMPO}$ signal among halogen-CN processes. However, with the increase of atomic number, the electronegativity of Cl, Br and I decreased. The electron of Cl, Br and I might migrate to the bulk CN, which reduce their selectiveness towards electrophilic O_3 [48]. Generation of H_2O_2 was also detected to investigate the reaction between O_2 and e^- (Fig. 6(c)). H_2O_2 was known as the important intermediate for the TER reaction of O_2 [19]. Therefore, the identical order of H_2O_2 accumulation amount with $\bullet\text{O}_2^-$ -DMPO intensity also served as evidence of the TER process. The interfacial electron transfer was investigated by photocurrents and linear sweep voltammetry curve (LSV) characterizations. Fig. 6(d) depicted that all halogen-CN had the greater photocurrents than that of CN. Photocurrent was resulted from the excitation of e^- by photons from VB to CB [49]. The enhancement of photocurrent could be ascribed to both the narrowing of E_g and the surface polarization of halogen-CN. As proposed by Teng, the polarized internal electric field within semiconductors could accelerate the e^- migration [50]. The differences of photocurrent indicated the increase of electronic polarization by doping halogens and the degree of electronic polarization was in the order of F-CN>I-CN>Br-CN>Cl-CN. LSV reflected that the introduction of O_2 had limited influence on the interfacial electron migration (Fig. 6(e)). The initial current of $\text{O}_2/\text{Vis/CN}$ and $\text{O}_2/\text{Vis/F-CN}$ were identical to those of CN and F-CN. However, after introducing O_3 , initial of current enhanced dramatically, which suggested that O_3 had the better activity with e^- than O_2 . Trend of initial currents of different CN based catalyst in PCO processes were consistent with order of intensity of $\bullet\text{OH}-\text{DMPO}$ signal (Fig. 6(f)), therefore, it further indicated that F-CN and I-CN had the better e^- utilization. Meanwhile, considering the potential reduction of $\text{O}_2/\text{H}_2\text{O}$ into singlet oxygen (${}^1\text{O}_2$, oxidation potential was -0.11 eV) by e^- , the generation of ${}^1\text{O}_2$ was also recorded by EPR with 2,2,6,6-tetramethylpiperidine-1-oxyl (TEMP) as probe agent [51]. However, the 1:1:1 triplet signal of TEMP- ${}^1\text{O}_2$ was hardly found for all PCO processes (Fig. S7). The above results were consistent with Xiao's reports, which thought that $\bullet\text{OH}$ and $\bullet\text{O}_2^-$ were the major ROSSs for PCO process [19].

The contributions of oxidative species to ATZ removal were also evaluated with TBA, DMSO, p-BQ, TEOA and KBrO₃ acting as scavengers for dissolved $\bullet\text{OH}$, surface $\bullet\text{OH}$, $\bullet\text{O}_2^-$, h^+ and e^- , respectively [52–54]. As depicted in Fig. 7, addition of most of the mentioned scavengers inhibited ATZ removal except for KBrO₃. The increase of ATZ removal with the co-existence of KBrO₃ suggested that more e^- was consumed by KBrO₃. Therefore, the recombination h^+-e^- was inhibited and the direct oxidation of h^+ was strengthened. KBrO₃ had the least impact on

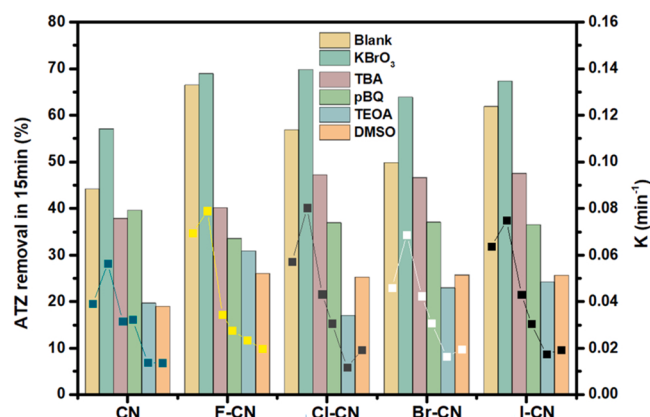


Fig. 7. Influence of scavenger on different PCO processes.

O_3 /Vis/F-CN process, which indirectly reflected the better e^- consumption on the surface of F-CN because of its greater affinity towards O_3 than that of Cl-CN, Br-CN, I-CN and CN. DMSO and TEOA had the greater inhibition rate than other kinds of scavengers for all investigated PCO processes. Therefore, it could be stated that h^+ and $\bullet OH$ (especially surface $\bullet OH$) played the more important role in degrading ATZ than $\bullet O_2^-$.

3.4. Theoretical calculation

DFT simulation was also employed to support the mentioned mechanism. For convenience discussion, the s-triazine rings in optimized structure were labeled as ring 1–4. Work function (Φ , $\Phi = E_{\text{Vac}} - E_F$) was calculated to illustrate the capacity of electron diffusion from catalyst [55,56]. E_{Vac} and E_F were the vacuum energy level and the electrostatic potential at the Fermi level, respectively. As showed in Fig. 8, E_F upshifted from -3.580 to -3.201 , -2.484 , -2.426 and -2.374 eV after doping CN with F, Cl, Br and I, respectively. With the increase of atomic number, the electronegativity of Cl, Br and I decrease. Therefore, the electron of halogen with greater atomic number might be transferred to CN, which upshifted the Fermi level [22]. E_{Vac} were 1.208 , 1.209 , 1.244 , 1.250 and 1.290 eV while Φ was calculated as 4.788 , 4.410 , 3.728 , 3.676 and 3.664 eV for CN, F-CN, Cl-CN, Br-CN and I-CN, respectively. The decrease of Φ with halogen doping suggested the more facility for the escaping of electron from CN surface.

LUMO and HOMO orbits of CN and halogen-CN were also investigated. As shown in Fig. 9, CN's HOMO was mainly composed by N2 atom and its LUMO was contributed by C1, C2 and N1 atom. The bridge N (N3) of CN did not participate in the HOMO and LUMO. Therefore, $h^+ - e^-$ was primarily generated at N2 sites and then e^- migrated to the adjacent atoms. Because of the insignificant contribution of N3 atom to both HOMO and LUMO, e^- was limited in a single s-triazine ring, which resulted in the low separation efficiency of $h^+ - e^-$ of CN. After doping with halogens, redistributions of HOMO and LUMO of halogen-CN were observed. Bridge N (N3) atom of halogen-CN all participated in HOMO and/or LUMO, which meant that e^- could migrate in the larger space. For F-CN, F was involved in the HOMO but did not contribute to the LUMO. Under the electron-withdrawing effect of F, electron on F-containing s-

triazine ring was delocalized. C1, C2, N3 and F in the F-containing s-triazine ring (ring 1) mainly contributed to HOMO. N1, N2 and C1 of ring 4 contributed a little to HOMO. LUMO were totally distributed outside of the fluorine-containing s-triazine ring. Therefore, the oxidation reaction occurred at F-containing s-triazine and reduction reaction happened at the neighboring s-triazine (ring 2–4). For the case of Cl-CN, Br-CN and I-CN, Cl, Br and I all participated in HOMO. Besides that, C1, C2, N1, N2 on the ring 1 as well as C1, C2, N1, N2 and N3 of ring 4 also contributed to HOMO. LUMO of Cl-CN, Br-CN and I-CN were contributed by both the halogen-free s-triazine ring (major) and the halogen-containing s-triazine ring (minor). The oxidation reaction occurred at ring 1 and 4 while reduction reaction happened at ring 3 for Cl, Br and I-CN. Electron localization function (ELF) results showed that CN had the highly conjugated structure, therefore, the highly symmetrical distribution of electrons was observed (Fig. 9). Doping of halogens had different influence on electron distribution. F on F-CN could seize the surrounding electron, building an electron-rich region centering C—F bond. However, electrons of Br and I migrated to bulk because of their decline of electronegativity, generating the electron-poor zone. As for Cl-CN, the electron migration was not as obvious as other kinds of halogen and its electron distribution was not highly polarized. The above results were echoed with the XPS.

The affinity of CN based catalysts towards O_2/O_3 were illustrated by calculating adsorption energy and the greater adsorption energy suggested their greater affinity [57]. Firstly, O_3 was placed on C1, C2, N1, N2 and N3 sites to find the possible sites of O_3^- adsorption on CN. Three ways of O_3^- 's adsorption were considered, namely horizontal adsorption via central oxygen atom, horizontal adsorption via edge oxygen atom and vertical adsorption via edge oxygen atom (shown in Fig. S8). As shown in Table S4, vertical adsorption of O_3 on N2 atom was the most favorable, with the maximum adsorption energy as -3.67 eV. The vertical adsorption model was adopted in subsequent work. O_2 adsorption energy at N2 of CN was -2.35 eV. During PCO process, O_3/O_2 should react with e^- at CB (LUMO orbit), hence, their adsorption sites on halogen-CN were more likely at N2 on ring 3 (Cl-CN, Br-CN and I-CN) and 4 (for F-CN), where were accumulated rich e^- at LUMO (Fig. S9). As shown in Table 4, compared with those of CN, both O_3 and O_2 adsorption energy on halogen-CN increased, which were attributed to their

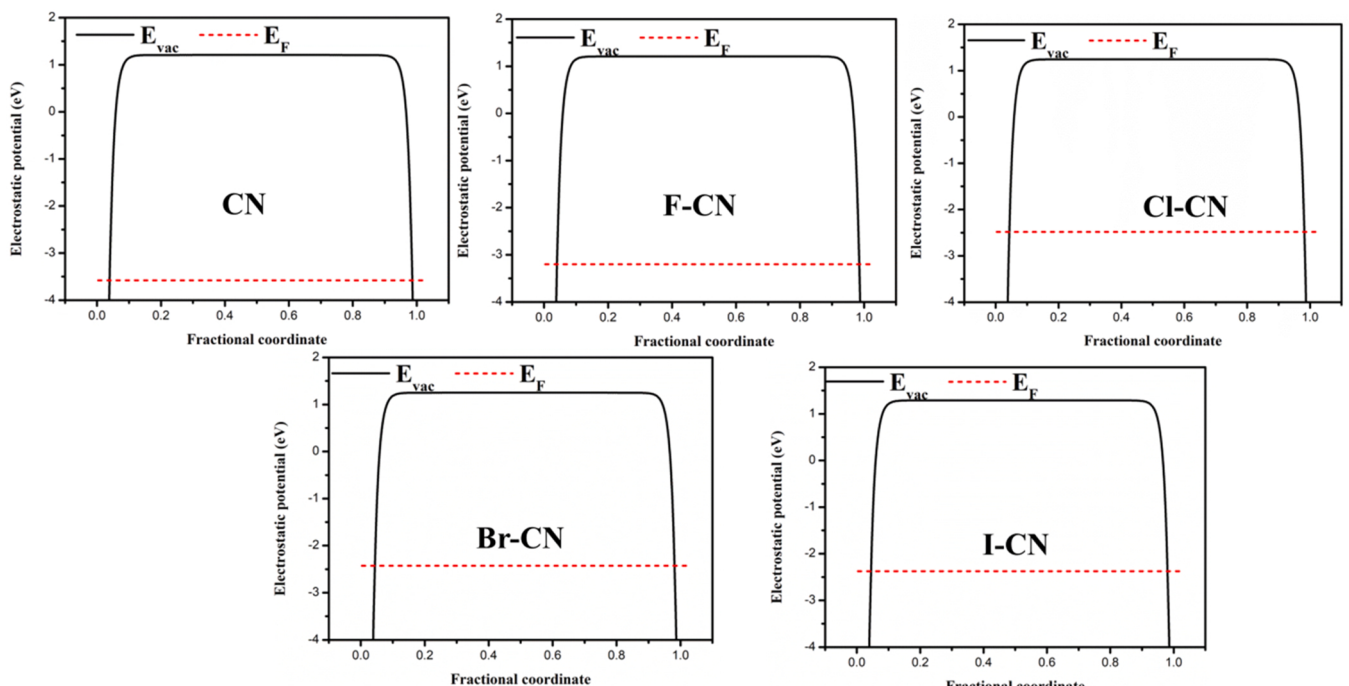


Fig. 8. Electrostatic potential profiles along z direction of CN and halogens-CN.

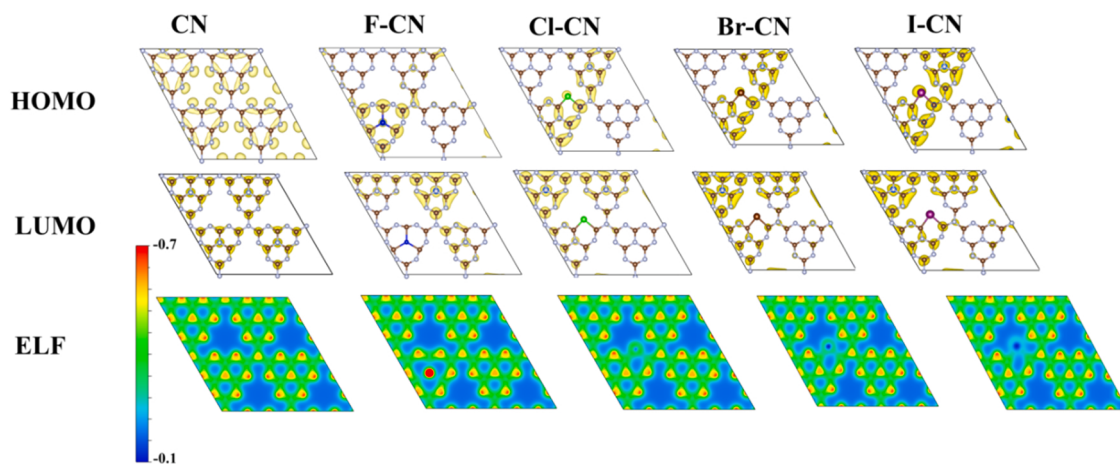


Fig. 9. Calculated HOMO, LUMO and electron localization function of CN and halogens-CN (isosurface value=0.05 e/Å).

Table 4
Adsorption energy of O₃/O₂ on CN and halogen-CN.

Catalysts	Adsorption energy (eV)	
	O ₃	O ₂
CN	-3.67	-2.35
F-CN	-5.53	-4.55
Cl-CN	-5.12	-6.77
Br-CN	-5.22	-6.79
I-CN	-5.48	-6.13

increase of hydrophobicity. O₃ adsorption energies were calculated as -5.53 , -5.12 , -5.22 , and -5.48 eV for F, Cl, Br and I-CN, respectively. O₂ adsorption energies were calculated as -4.55 , -6.77 , -6.79 , and -6.13 eV for F, Cl, Br and I-CN, respectively. Hydrophobic property of CN and halogen-CN were further characterized by water contact angle (CA). As depicted in Fig. S10, CA were 23.7 , 54.8 , 47.5 , 44.2 , and 37.8° for CN, F, Cl, Br and I-CN, which reflected the increase of hydrophobicity after halogen doping. Moreover, the residual ozone concentration was measured as 4.06 , 2.23 , 1.00 , 1.44 , 1.44 and 1.67 mg/L for sole ozonation, CN and F, Cl, Br, I-CN based PCO process (Fig. S11). Compared with those of CN-PCO process, the obvious decrease of residual ozone concentration in halogen-PCO processes suggested the greater O₃ utility rate, which might indirectly reflect the enhanced O₃ mass transfer and its subsequent reaction with e⁻. The greater O₂ desorption signal at 300°C were observed for halogen-CN over that of CN in O₂-TPD pattern, which reflected the greater O₂ adsorption capacity of halogen-CN over CN (Fig. S12). These results suggested that the strong adsorption of O₃/O₂ on F, Cl, Br and I-CN over CN facilitated the subsequent consumption of e⁻, which was favor for PCO [57]. O₃ adsorption energy of F-CN was the greatest among halogen-CN and it was also greater than O₂ adsorption energy. As proved in former parts, F on F-CN would construct electron rich zone, therefore, F-CN possessed greater affinity to electrophilic O₃. O₂ adsorption energy of Cl, Br and I-CN surpassed O₃ adsorption energy, which meant that they had the less selectiveness toward O₃ when compared with F-CN.

Basing on the experimental and calculating results, common advantages of halogen doping were summarized as that they all narrowed E_g, enhanced O₃/O₂'s mass transfer and enlarged space for e⁻ migration. The differences between halogens were depicted as following: (1) C-F in F-CN could withdraw electron from CN and construct both the hydrophobic sites and electron-rich region, which endowed F-CN with the selectivity towards O₃ and enhanced the SER reaction to generate more •OH. Meanwhile, C-F groups also downshifted F-CN's VB. Both h⁺ oxidation and •OH oxidation pathways were enhanced when compared with other kinds of CN; (2) C-Cl in Cl-CN had limited influence on the

electron polarization of CN, therefore, Cl-CN had less selectiveness towards O₃. Due to the competition of O₂'s TER reaction, the utilization rate of e⁻ might not as high as that of F-CN. But, the downshift of VB of Cl-CN could strengthen the direct oxidation ability of its h⁺; (3) Br-CN had the unfavorable CB and VB potential when compared with those of CN, therefore, its greater catalytic performance than CN might be lied in its narrower E_g and the greater amount of e⁻ on the surface to react with O₂ and O₃; (4) C-I in I-CN dramatically shifted its CB to upper position, which enhanced the reductive of e⁻ and the TER of O₂ and SER of O₃. The greater activity of I-CN than CN might be due to the generation of more •OH.

3.5. Degradation pathway of ATZ and change of toxicity

Generation of by-products during O₃/Vis/F-CN was measured by LC-MS/MS for deducing ATZ degradation pathway. About 16 kinds of by-products were detected and their structures were further confirmed by secondary mass spectrometry (Table S5 and Figs. S13–31). Dealkylation, dechlorination, hydroxylation, alkyl oxidation, alkyl hydroxylation and olefination were main reactions during ATZ oxidation, which were also summarized by reported literatures [58,59]. Basing on the detected components, four possible degradation pathways were deduced and depicted in Fig. 10(a). Pathway 1 and 4 were dominated by •OH oxidation. In pathway 1, DEX was first attack by •OH and one side chain or both side chains of ATZ were hydroxylated, which then generated CNIT and CHTE. Then CNIT was served as precursor of CDIT via the alkyl oxidation and finally generated CDHT after the further oxidation by •OH. Meanwhile, CVIT also formed from the olefination of CNIT. CVAT was obtained after CVIT's dealkylation. In pathway 4, •OH attack Cl group directly and generated the hydroxylated products, namely DEIT. The step by step dechlorination was happened on both sides' chains of DEIT, generating DEAT, DAIT and DAAT. Because amino groups of DAAT were reductive, DAAT was easily oxidized to DRT accompanying with oxidation of -NH₂ to -NO₂ groups. As for pathway 2 and 3, it might be dominated by h⁺ and •O₂⁻. Due to their strong electronegativity, N atoms on both side chains were electron-rich and were likely to be oxidized by h⁺. Therefore, alkyl groups of ATZ were eliminated progressively to form CEAT, CAIT and CAAT. As proposed by Ye, during the dealkylation of ATZ to CEAT and CAIT, carbon-center radicals were also generated because of the H extraction on the α-C next to N. The carbon-center radicals were consequently oxidized by •O₂⁻, which finally generated CAAT [60]. However, because of the lack of powerful equipment, the above hypothesis could only be proved by detecting the corresponding product. After that, one of CAAT's amino groups was oxidized, generating CANT. Hydroxylation and dehalogenation were also likely to happen for CAAT, and generated DAAT.

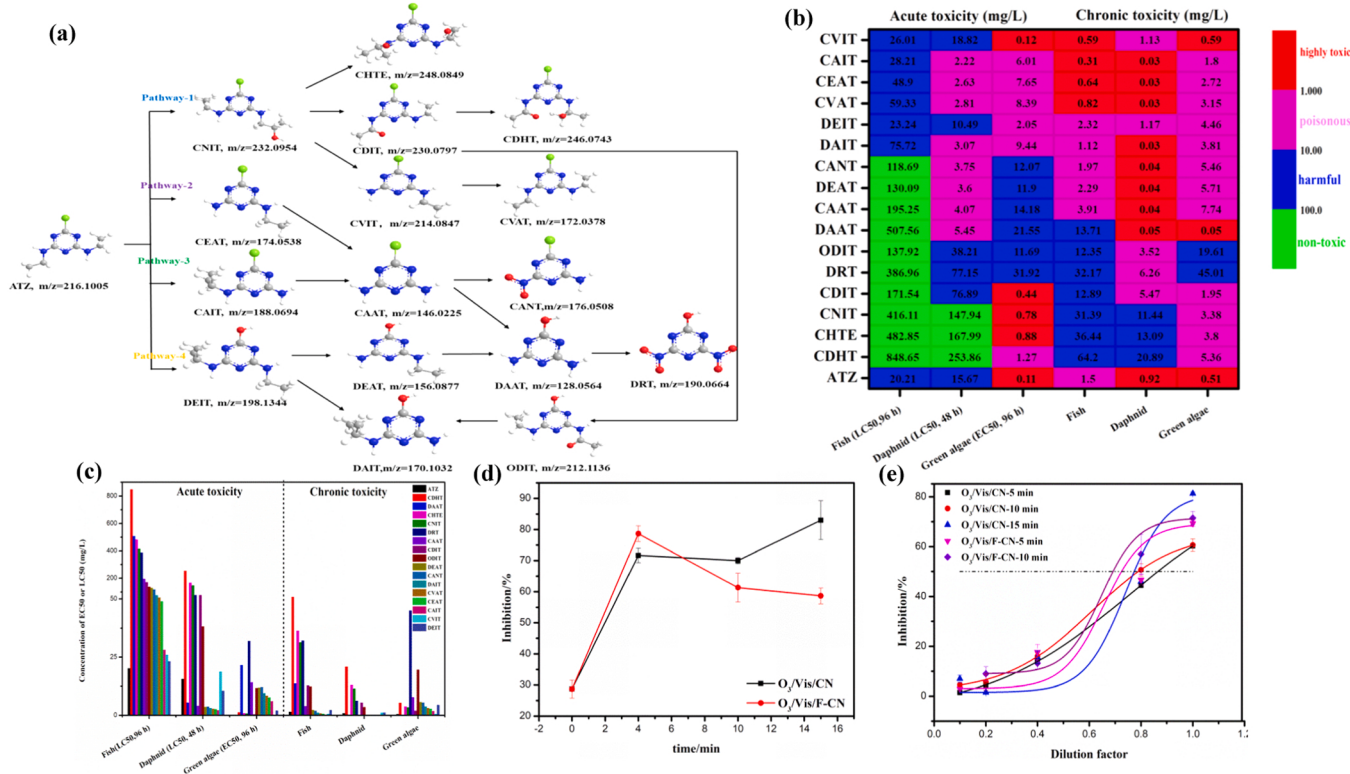


Fig. 10. (a) Proposed degradation pathway, (b-c) predicted acute and chronic toxicity of by-products, (d-e) acute toxicity of by-products on photobacterium luminescens.

ECOSAR was employed to explore the toxicity of intermediates (both acute and chronic). By referring to the LC50, EC50 and ChV values, their toxicity could be divided into: highly toxic (<1.0 mg/L), toxic (1.0–10.0 mg/L), harmful (10.0–100.0 mg/L) and harmless (>100.0 mg/L) [61]. As exhibited in Fig. 10(b-c), for the case of acute toxicity, ATZ was highly toxic to green algae but only harmful to fish and daphnid. For the case of chronic toxicity, ATZ was poisonous to fish but highly toxic for both daphnid and green algae. ATZ and its intermediates had the more significant impact on daphnid and green algae than that on fish. After the degradation, toxicity of intermediates varied with each other depending on testing species. LC50 towards fish of all intermediates increased when compared with that of ATZ during the acute toxicity test. 62.5% of intermediates were non-toxic and 37.5% of intermediates were still harmful to fish. As for chronic toxicity to fish, 43.8% of intermediates were harmful, 33.3% of intermediates were poisonous while the rest 25.0% were highly toxic. When choosing daphnid as testing species, non-toxic, harmful and poisonous intermediates accounted for 18.8%, 31.2% and 50.0% during acute toxicity test. But harmful, poisonous and highly toxic species accounted for 18.8%, 31.2% and 50.0% during chronic toxicity test. ATZ and its intermediates had the greatest impact on green algae. Though the increase of EC50 value on algae, 4 kinds of ATZ-derivatives were still high toxic, 6 kinds of the intermediates were poisonous and 6 kinds of intermediates were harmful. As for the chronic toxicity test, DAAT and CVIT were found highly toxic, DRT and ODIT were harmful, and the remaining 12 kinds of derivatives were all poisonous to algae. For summarizing the above results, intermediates in pathway 1 and 4 were less risk than those in pathway 2 and 3. The mixed acute toxicity of intermediates during $O_3/\text{Vis/CN}$ and $O_3/\text{Vis/F-CN}$ were tested with photobacterium luminescens as test organism. As shown in Fig. 10(d-e), the inhibition rate of ATZ towards photobacterium luminescens was 28.7% and samples in both $O_3/\text{Vis/CN}$ and $O_3/\text{Vis/F-CN}$ processes had the much greater inhibition rates, which suggested the greater toxicity of intermediates. In $O_3/\text{Vis/CN}$ process, the toxicity of intermediates

gradually increased with degradation time. But it had an initial increase and then decreased in $O_3/\text{Vis/F-CN}$ process. The toxicity of intermediates in $O_3/\text{Vis/F-CN}$ was less than that in $O_3/\text{Vis/CN}$ process except in the first 5 min. The EC50 value in both processes shifted to the smaller dilution factor with the proceeding of degradation and the toxic of by-products in $O_3/\text{Vis/F-CN}$ was much smaller than those of $O_3/\text{Vis/CN}$. Though the obvious advantage of F-CN over CN, the completely detoxification of ATZ required more attentions in further study.

4. Conclusions

Halogen incorporated CN (F, Cl, Br and I-CN) were prepared to accelerate ATZ degradation during photocatalytic ozonation process. All halogen-CN had the better activity than CN and their activity was in the order of F-CN>I-CN>Cl-CN>Br-CN>CN. C-halogen bond could narrow E_g , enhance mass transfer of O_3 and/or O_2 and redistribute the ingredient of HOMO and LUMO to provide the larger space for e^- migration. Besides the above advantages, they could also either upshift CB (C-I) or downshift VB (C-F and C-Cl) to enhance h^+ direct oxidation and $\bullet\text{OH}$'s indirect oxidation. h^+ and surface $\bullet\text{OH}$ played the major role for degrading ATZ in all CN assisted photocatalytic ozonation processes. Basing on the LC-MS/MS results, 16 kinds of by-products were detected and 4 degradation pathways were deduced. This study could serve as guiding for designing cost-effective catalyst for photocatalytic ozonation process.

CRediT authorship contribution statement

Yushan Tan: Methodology. **Weirui Chen:** Conceptualization, Methodology, Writing – original draft. **Gaozu Liao:** Methodology. **Xukai Li:** Supervision, Validation. **Jing Wang:** Funding acquisition. **Yiming Tang:** Funding acquisition. **Laisheng Li:** Writing – review & editing, Funding acquisition.

Declaration of Competing Interest

The authors declare that they have no known competing financial interests or personal relationships that could have appeared to influence the work reported in this paper.

Acknowledgments

This study was funded by National Natural Science Foundation (51978288, 52000079 and 22076050), Guangdong Basic and Applied Basic Research Foundation (2021A1515111143), Guangzhou Science and Technology Project (202102020062) and Cultivate Fund of South China Normal University (20KJ11).

Appendix A. Supplementary material

Supplementary data associated with this article can be found in the online version at doi:10.1016/j.apcatb.2022.121133.

References

- [1] M. Bayati, M. Numaan, A. Kadhem, Z. Salahshoor, S. Qasim, H. Deng, J. Lin, Z. Yan, C.-H. Lin, M. Fidalgo de Cortalezzi, Adsorption of atrazine by laser induced graphitic material: an efficient, scalable and green alternative for pollution abatement, *J. Environ. Chem. Eng.* 8 (2020), 104407.
- [2] Z. Wang, W. Ouyang, M. Tysklind, C. Lin, B. Wang, Seasonal variations in atrazine degradation in a typical semienclosed bay of the northwest Pacific ocean, *Environ. Pollut.* 283 (2021), 117072.
- [3] M. Triassi, P. Montuori, D.P. Provisiero, E. De Rosa, F. Di Duca, P. Sarnacchiaro, S. Diez, Occurrence and spatial-temporal distribution of atrazine and its metabolites in the aquatic environment of the Volturno River estuary, southern Italy, *Sci. Total Environ.* 803 (2021), 149972.
- [4] X. Liu, H. Zong, X. Tan, X. Wang, J. Qiu, F. Kong, J. Zhang, S. Fang, Facile synthesis of modified carbon nitride with enhanced activity for photocatalytic degradation of atrazine, *J. Environ. Chem. Eng.* 9 (2021), 105807.
- [5] J. Nawrocki, B. Kasprzyk-Hordern, The efficiency and mechanisms of catalytic ozonation, *Appl. Catal. B Environ.* 99 (2010) 27–42.
- [6] W. Li, X. Lu, K. Xu, J. Qu, Z. Qiang, Cerium incorporated MCM-48 (Ce-MCM-48) as a catalyst to inhibit bromate formation during ozonation of bromide-containing water: efficacy and mechanism, *Water Res.* 86 (2015) 2–8.
- [7] G. Yu, Y. Wang, H. Cao, H. Zhao, Y. Xie, Reactive oxygen species and catalytic active sites in heterogeneous catalytic ozonation for water purification, *Environ. Sci. Technol.* 54 (2020) 5931–5946.
- [8] U. von Gunten, Ozonation of drinking water: part II. Disinfection and by-product formation in presence of bromide, iodide or chlorine, *Water Res.* 37 (2003) 1469–1487.
- [9] U. von Gunten, Ozonation of drinking water: part I. Oxidation kinetics and product formation, *Water Res.* 37 (2003) 1443–1467.
- [10] S. Afzal, X. Quan, S. Lu, Catalytic performance and an insight into the mechanism of CeO₂ nanocrystals with different exposed facets in catalytic ozonation of p-nitrophenol, *Appl. Catal. B Environ.* 248 (2019) 526–537.
- [11] Y. Huang, M. Luo, S. Li, D. Xia, Z. Tang, S. Hu, S. Ye, M. Sun, C. He, D. Shu, Efficient catalytic activity and bromate minimization over lattice oxygen-rich MnOOH nanorods in catalytic ozonation of bromide-containing organic pollutants: lattice oxygen-directed redox cycle and bromate reduction, *J. Hazard. Mater.* 410 (2021), 124545.
- [12] C. Cai, X. Duan, X. Xie, S. Kang, C. Liao, J. Dong, Y. Liu, S. Xiang, D.D. Dionysiou, Efficient degradation of clofibric acid by heterogeneous catalytic ozonation using CoFe₂O₄ catalyst in water, *J. Hazard. Mater.* 410 (2021), 124604.
- [13] J. Yang, Y. Huang, Y.-W. Chen, D. Xia, C.-Y. Mou, L. Hu, J. Zeng, C. He, P.K. Wong, H.-Y. Zhu, Active site-directed tandem catalysis on CuO/V₂O₅-MnO₂ for efficient and stable catalytic ozonation of S-VOCs under mild condition, *Nano Today* 35 (2020), 100944.
- [14] D. Xia, W. Xu, Y. Wang, J. Yang, Y. Huang, L. Hu, C. He, D. Shu, D.Y.C. Leung, Z. Pang, Enhanced performance and conversion pathway for catalytic ozonation of methyl mercaptan on single-atom Ag deposited three-dimensional ordered mesoporous MnO₂, *Environ. Sci. Technol.* 52 (2018) 13399–13409.
- [15] M. Checa, M. Figueredo, A. Aguinaco, F.J. Beltran, Graphene oxide/titania photocatalytic ozonation of primidone in a visible LED photoreactor, *J. Hazard. Mater.* 369 (2019) 70–78.
- [16] D. Xia, H. He, H. Liu, Y. Wang, Q. Zhang, Y. Li, A. Lu, C. He, P.K. Wong, Persulfate-mediated catalytic and photocatalytic bacterial inactivation by magnetic natural ilmenite, *Appl. Catal. B Environ.* 238 (2018) 70–81.
- [17] J.F. Gomes, A. Lopes, M. Gmurek, R.M. Quinta-Ferreira, R.C. Martins, Study of the influence of the matrix characteristics over the photocatalytic ozonation of parabens using Ag-TiO₂, *Sci. Total Environ.* 646 (2019) 1468–1477.
- [18] X. Chen, S. Zhan, D. Chen, C. He, S. Tian, Y. Xiong, Grey Fe-CeO₂- α for boosting photocatalytic ozonation of refractory pollutants: roles of surface and bulk oxygen vacancies, *Appl. Catal. B Environ.* 286 (2021), 119928.
- [19] J. Xiao, Y. Xie, J. Rabeh, A. Bruckner, H. Cao, Visible-light photocatalytic ozonation using graphitic C₃N₄ catalysts: a hydroxyl radical manufacturer for wastewater treatment, *Acc. Chem. Res.* 53 (2020) 1024–1033.
- [20] J. Xiao, J. Rabeh, J. Yang, Y. Xie, H. Cao, A. Brückner, Fast electron transfer and •OH formation: key features for high activity in visible-light-driven ozonation with C₃N₄ catalysts, *ACS Catal.* 7 (2017) 6198–6206.
- [21] J. Xiao, Y. Xie, F. Nawaz, S. Jin, F. Duan, M. Li, H. Cao, Super synergy between photocatalysis and ozonation using bulk g-C₃N₄ as catalyst: a potential sunlight/O₃/g-C₃N₄ method for efficient water decontamination, *Appl. Catal. B Environ.* 181 (2016) 420–428.
- [22] B. Zhu, J. Zhang, C. Jiang, B. Cheng, J. Yu, First principle investigation of halogen-doped monolayer g-C₃N₄ photocatalyst, *Appl. Catal. B Environ.* 207 (2017) 27–34.
- [23] J. Yang, Y. Chen, P. Xu, Y. Li, X. Jia, H. Song, Fabrication of compressible and underwater superoleophobic carbon/g-C₃N₄ aerogel for wastewater purification, *Mater. Lett.* 254 (2019) 210–213.
- [24] X. Hu, Y. Zhang, B. Wang, H. Li, W. Dong, Novel g-C₃N₄/BiOCl_xI_{1-x} nanosheets with rich oxygen vacancies for enhanced photocatalytic degradation of organic contaminants under visible and simulated solar light, *Appl. Catal. B Environ.* 256 (2019), 117789.
- [25] C. Chen, H. Zeng, M. Yi, G. Xiao, S. Xu, S. Shen, B. Feng, In-situ growth of Ag₃PO₄ on calcined Zn-Al layered double hydroxides for enhanced photocatalytic degradation of tetracycline under simulated solar light irradiation and toxicity assessment, *Appl. Catal. B Environ.* 252 (2019) 47–54.
- [26] W. Chen, Y. Bao, X. Li, J. Huang, J. Xie, L. Li, Role of SiF groups in enhancing interfacial reaction of Fe-MCM-41 for pollutant removal with ozone, *J. Hazard. Mater.* 393 (2020), 122387.
- [27] F. Wang, P. Chen, Y. Feng, Z. Xie, Y. Liu, Y. Su, Q. Zhang, Y. Wang, K. Yao, W. Lv, G. Liu, Facile synthesis of N-doped carbon dots/g-C₃N₄ photocatalyst with enhanced visible-light photocatalytic activity for the degradation of indomethacin, *Appl. Catal. B Environ.* 207 (2017) 103–113.
- [28] W.-J. Jong, L.-L. Tan, S.-P. Chai, S.-T. Yong, Graphene oxide as a structure-directing agent for the two-dimensional interface engineering of sandwich-like graphene/g-C₃N₄ hybrid nanostructures with enhanced visible-light photoreduction of CO₂ to methane, *Chem. Commun.* 51 (2015) 858–861.
- [29] X.-H. Li, J. Zhang, X. Chen, A. Fischer, A. Thomas, M. Antonietti, X. Wang, Condensed graphic carbon nitride nanorods by nanoconfinement: promotion of crystallinity on photocatalytic conversion, *Chem. Mater.* 23 (2011) 4344–4348.
- [30] F. Dong, L. Wu, Y. Sun, M. Fu, Z. Wu, S.C. Lee, Efficient synthesis of polymeric g-C₃N₄ layered materials as novel efficient visible light driven photocatalysts, *J. Mater. Chem. C* 21 (2011) 15171.
- [31] X.-C. Yang, Y.-L. Yang, S.-L. Zhang, Y.-F. Liu, S.-J. Fu, M. Zhu, J.-F. Hu, Z.-J. Zhang, J.-T. Zhao, Facile synthesis of porous nitrogen doped carbon dots (NCDs)@g-C₃N₄ for highly efficient photocatalytic and anti-counterfeiting applications, *Appl. Surf. Sci.* 490 (2019) 592–597.
- [32] J. Zhang, B. Xin, C. Shan, W. Zhang, D.D. Dionysiou, B. Pan, Roles of oxygen-containing functional groups of O-doped g-C₃N₄ in catalytic ozonation: quantitative relationship and first-principles investigation, *Appl. Catal. B Environ.* 292 (2021), 120155.
- [33] J. Wang, S. Chen, X. Quan, H. Yu, Fluorine-doped carbon nanotubes as an efficient metal-free catalyst for destruction of organic pollutants in catalytic ozonation, *Chemosphere* 190 (2018) 135–143.
- [34] N.X.-r.P.S Database, NIST Standard Reference Database Number 20, National Institute of Standards and Technology, Gaithersburg MD, 20899, 2000. DOI: 10.18434/T18434T18488K.
- [35] Y. Hu, Y. Shim, J. Oh, S. Park, S. Park, Y. Ishii, Synthesis of 13C-,15N-labeled graphitic carbon nitrides and NMR-based evidence of hydrogen-bonding assisted two-dimensional assembly, *Chem. Mater.* 29 (2017) 5080–5089.
- [36] R. Jiang, G. Lu, J. Liu, D. Wu, Z. Yan, Y. Wang, Incorporation of π-conjugated molecules as electron donors in g-C₃N₄ enhances photocatalytic H₂-production, *Renew. Energy* 164 (2021) 531–540.
- [37] Y. Wang, Y. Zhang, S. Zhao, Z. Huang, W. Chen, Y. Zhou, X. Lv, S. Yuan, Bio-template synthesis of Mo-doped polymer carbon nitride for photocatalytic hydrogen evolution, *Appl. Catal. B Environ.* 248 (2019) 44–53.
- [38] F. Zhang, J. Liao, J. Lu, J. Niu, Extensive incorporation of carboxyl groups into g-C₃N₄ by integrated oxygen doping and HNO₃ oxidation for enhanced catalytic ozonation of para-chlorobenzoic acid and atrazine, *Sep. Purif. Technol.* 256 (2021), 117806.
- [39] K. Guo, Z. Wu, S. Yan, B. Yao, W. Song, Z. Hua, X. Zhang, X. Kong, X. Li, J. Fang, Comparison of the UV/chlorine and UV/H₂O₂ processes in the degradation of PPCPs in simulated drinking water and wastewater: kinetics, radical mechanism and energy requirements, *Water Res.* 147 (2018) 184–194.
- [40] L. Ruan, G. Xu, L. Gu, C. Li, Y. Zhu, Y. Lu, The physical properties of Li-doped g-C₃N₄ monolayer sheet investigated by the first-principles, *Mater. Res. Bull.* 66 (2015) 156–162.
- [41] Y. Yang, B. Mao, G. Gong, D. Li, Y. Liu, W. Cao, L. Xing, J. Zeng, W. Shi, S. Yuan, In-situ growth of Zn-AgInS₂ quantum dots on g-C₃N₄ towards OD/2D heterostructured photocatalysts with enhanced hydrogen production, *Int. J. Hydron. Energy* 44 (2019) 15882–15891.
- [42] L. Duan, B. Wang, K. Heck, S. Guo, C.A. Clark, J. Arredondo, M. Wang, T.P. Senftle, P. Westerhoff, X. Wen, Y. Song, M.S. Wong, Efficient photocatalytic PFOA degradation over boron nitride, *Environ. Sci. Technol.* 54 (2020) 613–619.
- [43] Z. Song, X. Dong, N. Wang, L. Zhu, Z. Luo, J. Fang, C. Xiong, Efficient photocatalytic defluorination of perfluorooctanoic acid over BiOCl nanosheets via a hole direct oxidation mechanism, *Chem. Eng. J.* 317 (2017) 925–934.

- [44] J. Xiao, Y. Xie, H. Cao, Y. Wang, Z. Guo, Y. Chen, Towards effective design of active nanocarbon materials for integrating visible-light photocatalysis with ozonation, *Carbon* 107 (2016) 658–666.
- [45] S.Q. Tian, J.Y. Qi, Y.P. Wang, Y.L. Liu, L. Wang, J. Ma, Heterogeneous catalytic ozonation of atrazine with Mn-loaded and Fe-loaded biochar, *Water Res.* 193 (2021), 116860.
- [46] Q. Wang, B. Wang, Y. Ma, S. Xing, Enhanced superoxide radical production for ofloxacin removal via persulfate activation with Cu-Fe oxide, *Chem. Eng. J.* 354 (2018) 473–480.
- [47] P. Peluso, V. Mamane, A. Densi, R. Dallochio, E. Aubert, C. Gatti, D. Mangelings, S. Cossu, Halogen bond in separation science: a critical analysis across experimental and theoretical results, *J. Chromatogr. A* 2020 (1616), 460788.
- [48] S. Patnaik, D.P. Sahoo, K. Parida, Recent advances in anion doped g-C₃N₄ photocatalysts: a review, *Carbon* 172 (2021) 682–711.
- [49] K. Li, Y. Liang, H. Yang, S. An, H. Shi, C. Song, X. Guo, New insight into the mechanism of enhanced photo-Fenton reaction efficiency for Fe-doped semiconductors: a case study of Fe/g-C₃N₄, *Catal. Today* 371 (2021) 58–63.
- [50] Z. Teng, N. Yang, H. Lv, S. Wang, M. Hu, C. Wang, D. Wang, G. Wang, Edge-functionalized g-C₃N₄ nanosheets as a highly efficient metal-free photocatalyst for safe drinking water, *Chem* 5 (2019) 664–680.
- [51] D. Xia, H. Liu, B. Xu, Y. Wang, Y. Liao, Y. Huang, L. Ye, C. He, P.K. Wong, R. Qiu, Single Ag atom engineered 3D-MnO₂ porous hollow microspheres for rapid photothermocatalytic inactivation of *E. coli* under solar light, *Appl. Catal. B Environ.* 245 (2019) 177–189.
- [52] L.-F. Zhai, M.-F. Duan, M.-X. Qiao, M. Sun, S. Wang, Electro-assisted catalytic wet air oxidation of organic pollutants on a MnO@C/GF anode under room condition, *Appl. Catal. B Environ.* 256 (2019), 117822.
- [53] J.J. Du, Y.P. Yuan, J.X. Sun, F.M. Peng, X. Jiang, L.G. Qiu, A.J. Xie, Y.H. Shen, J. F. Zhu, New photocatalysts based on MIL-53 metal-organic frameworks for the decolorization of methylene blue dye, *J. Hazard. Mater.* 190 (2011) 945–951.
- [54] Z. Li, S. Li, Y. Tang, X. Li, J. Wang, L. Li, Highly efficient degradation of perfluorooctanoic acid: an integrated photo-electrocatalytic ozonation and mechanism study, *Chem. Eng. J.* 391 (2020), 123533.
- [55] J. Liu, B. Cheng, J. Yu, A new understanding of the photocatalytic mechanism of the direct Z-scheme g-C₃N₄/TiO₂ heterostructure, *Phys. Chem. Chem. Phys. PCCP* 18 (2016) 31175–31183.
- [56] J. Liu, Origin of high photocatalytic efficiency in monolayer g-C₃N₄/CdS heterostructure: a hybrid DFT study, *J. Phys. Chem. C* 119 (2015) 28417–28423.
- [57] C. He, Y. Wang, Z. Li, Y. Huang, Y. Liao, D. Xia, S. Lee, Facet engineered alpha-MnO₂ for efficient catalytic ozonation of odor CH₃SH: oxygen vacancy-induced active centers and catalytic mechanism, *Environ. Sci. Technol.* 54 (2020) 12771–12783.
- [58] S. Zhu, B. Dong, Y. Yu, L. Bu, J. Deng, S. Zhou, Heterogeneous catalysis of ozone using ordered mesoporous Fe₃O₄ for degradation of atrazine, *Chem. Eng. J.* 328 (2017) 527–535.
- [59] J. Li, Y. Wan, Y. Li, G. Yao, B. Lai, Surface Fe(III)/Fe(II) cycle promoted the degradation of atrazine by peroxymonosulfate activation in the presence of hydroxylamine, *Appl. Catal. B Environ.* 256 (2019), 117782.
- [60] G. Ye, P. Luo, Y. Zhao, G. Qiu, Y. Hu, S. Preis, C. Wei, Three-dimensional Co/Ni bimetallic organic frameworks for high-efficient catalytic ozonation of atrazine: mechanism, effect parameters, and degradation pathways analysis, *Chemosphere* 253 (2020), 126767.
- [61] X. Xu, J. Chen, R. Qu, Z. Wang, Oxidation of tris (2-chloroethyl) phosphate in aqueous solution by UV-activated peroxymonosulfate: kinetics, water matrix effects, degradation products and reaction pathways, *Chemosphere* 185 (2017) 833–843.